OPEN ACCESS



GRB 190829A—A Showcase of Binary Late Evolution

Yu Wang^{1,2,3}, J. A. Rueda^{1,2,4,5,6}, R. Ruffini^{1,2,7}, R. Moradi^{1,2,3}, Liang Li^{1,2,3}, Y. Aimuratov^{1,2,8,15}, F. Rastegarnia^{2,5,9}, S. Eslamzadeh^{2,5,10}, N. Sahakyan¹¹, and Yunlong Zheng^{2,12,13,14} ¹ ICRA, Dip. di Fisica, Università di Roma "La Sapienza", Piazzale Aldo Moro 5, I-00185 Roma, Italy;yu.wang@uniroma1.it, jorge.rueda@icra.it, ruffini@icra.it, rahim.moradi@inaf.it, liang.li@icranet.org ² ICRANet, Piazza della Repubblica 10, I-65122 Pescara, Italy ³ INAF—Osservatorio Astronomico d'Abruzzo, Via M. Maggini snc, I-64100 Teramo, Italy ⁴ ICRANet-Ferrara, Dip. di Fisica e Scienze della Terra, Università degli Studi di Ferrara, Via Saragat 1, I-44122 Ferrara, Italy Dip. di Fisica e Scienze della Terra, Università degli Studi di Ferrara, Via Saragat 1, I-44122 Ferrara, Italy INAF, Istituto di Astrofisica e Planetologia Spaziali, Via Fosso del Cavaliere 100, I-00133 Rome, Italy INAF, Viale del Parco Mellini 84, I-00136 Rome, Italy ⁸ Fesenkov Astrophysical Institute, Observatory 23, 050020 Almaty, Kazakhstan ⁹ Department of Physics, Faculty of Physics and Chemistry, Alzahra University, Tehran, Iran Department of Theoretical Physics, Faculty of Basic Sciences, University of Mazandaran, P.O. Box 47416-95447, Babolsar, Iran ICRANet-Armenia, Marshall Baghramian Avenue 24a, Yerevan 0019, Armenia 12 Department of Astronomy, School of Physical Sciences, University of Science and Technology of China, Hefei, Anhui 230026, People's Republic of China 13 CAS Key Laboratory for Researches in Galaxies and Cosmology, University of Science and Technology of China, Hefei, Anhui 230026, People's Republic of China

School of Astronomy and Space Science, University of Science and Technology of China, Hefei, Anhui 230026, People's Republic of China al-Farabi Kazakh National University, al-Farabi Avenue 71, 050040 Almaty, Kazakhstan; rahim.moradi@inaf.it Received 2022 March 3; revised 2022 June 4; accepted 2022 June 29; published 2022 September 14

Abstract

GRB 190829A is the fourth-closest gamma-ray burst to date (z = 0.0785). Owing to its wide range of radio, optical, X-ray, and very-high-energy observations by HESS, it has become an essential new source that has been examined by various models with complementary approaches. Here, we show in GRB 190829A that the double prompt pulses and the three multiwavelength afterglows are consistent with the type II binary-driven hypernova model. The progenitor is a binary composed of a carbon–oxygen (CO) star and a neutron star (NS) companion. The gravitational collapse of the iron core of the CO star produces a supernova (SN) explosion and leaves behind a new NS (ν NS) at its center. The accretion of the SN ejecta onto the NS companion and onto the ν NS via matter fallback spins up the NSs and produces the double-peak prompt emission. The synchrotron emission from the expanding SN ejecta, with energy injection from the rapidly spinning ν NS and its subsequent spindown, leads to the afterglow in the radio, optical, and X-ray bands. We model the sequence of physical and related radiation processes in BdHNe, and focus on individuating the binary properties that play the relevant roles.

Unified Astronomy Thesaurus concepts: Gamma-ray bursts (629); Black hole physics (159); Neutron stars (1108); Supernovae (1668); Type Ic supernovae (1730)

1. Introduction

As one of the closest gamma-ray bursts (GRBs; Dichiara et al. 2019; Heintz et al. 2019; Hu et al. 2021), GRB 190829A has been the subject of one of the most extensive observational campaigns, including but not limited to the Fermi satellite (Fermi GBM Team 2019), the Neil Gehrels Swift Observatory (Perley & Cockeram 2019), the High Energy Stereoscopic System (HESS; Abdalla et al. 2021), the Gran Telescopio Canarias (GTC; de Ugarte Postigo et al. 2019), and the Gamma-Ray Burst Optical/Near-Infrared Detector (GROND; Bolmer et al. 2019). GRB 190829A has become a key source for testing details of alternative GRB models. The conventional concept of GRBs postulates that when the core of a single massive star collapses, a relativistic jet-like outflow forms and propagates. The internal shock in the outflow produces prompt emissions. The outflow then interacts with the interstellar medium, generating the afterglow via the synchrotron process, as well as the very-high-energy (VHE) emission via the

Original content from this work may be used under the terms of the Creative Commons Attribution 4.0 licence. Any further distribution of this work must maintain attribution to the author(s) and the title of the work, journal citation and DOI.

synchrotron self-Compton (SSC) process (Mészáros 2002; Piran 2004; Zhang 2018; Abdalla et al. 2019; MAGIC Collaboration et al. 2019; Zhang 2019; Abdalla et al. 2021). Here, we present an alternative approach: the progenitor is a binary system composed of a carbon-oxygen core (CO_{core}) and a companion neutron star (NS) in a tight orbit with an orbital period of a few minutes. The iron core of the CO_{core} collapses and generates a supernova (SN) at the end of its thermonuclear evolution, with a new NS (ν NS) being left at the SN's center. The accretion of SN ejecta onto the companion NS and the fallback accretion onto the νNS contribute to the energy of prompt emission, spinning up the ν NS. The rotational energy from the ν NS spindown powers the afterglow of the synchrotron emission (Rueda & Ruffini 2012; Fryer et al. 2014; Becerra et al. 2019; Rueda et al. 2021; Ruffini et al. 2021). The observed optical SN (Perley & Cockeram 2019; de Ugarte Postigo et al. 2019) completes this alternative selfconsistent approach.

Specifically, Abdalla et al. (2021) presented the HESS observations of VHE photons of hundreds of GeV, lasting 10⁵ s. The VHE photons exhibit a luminosity decaying index and a spectral shape similar to the ones of the X-ray afterglow emission. The standard forward-shock model was applied to the afterglow, revealing its difficulties in explaining these

observations. Rhodes et al. (2020) showed that the radio observations could be explained within the synchrotron forward-shock model. Hu et al. (2021) presented the optical observations, analyzed the multiwavelength data, and compared this burst with GRB 180728A. Fraija et al. (2021) modeled the optical and X-ray observations in the afterglow using the synchrotron forward-shock model, and the VHE observations with SSC scattering. Zhang et al. (2021a) interpreted the VHE observations using the external inverse-Compton scenario, with the seed photons coming from prompt emission pulses. Chand et al. (2020) analyzed various episodes of this burst and concluded that the shockwave breakout model could not explain the entire burst. Sato et al. (2021) proposed that this GRB was being viewed from an off-axis angle, in an attempt to solve the dilemma of the VHE photons being produced in a low-luminosity GRB. Zhang et al. (2021b) proposed that the interaction of the hard X-ray photons in the first prompt pulse with the dusty medium produces the second prompt pulse, as well as a medium rich in electron-positron pairs, in which the SSC process produces the VHE emission. Dichiara et al. (2021) focused on the early afterglow, with their multiwavelength studies purporting the existence of both forward and reverse shocks.

The above articles present detailed observations, including radio, optical, X-ray, and VHE, and give a variety of interpretations of the different emission episodes: they all generally assume a single progenitor and ultrarelativistic shock waves. In this article, we start by focusing on the nature of the binary progenitor, and far from describing a single leading ultrarelativistic process, we emphasize the existence of a number of episodes with different emission processes, which we examine in their rest-frames. We do not evidence any ultrarelativistic emission. On the contrary, we evidence: (1) the special role of two early pulses, observed by Fermi and Swift, relating to the progenitors of binary components; (2) the crucial role of synchrotron electromagnetic radiation from the mildrelativistic expanding SN ejecta in describing the afterglow composed of radio, optical, and X-ray emissions; and (3) we finally address the appearance of the SN, for which the optical emission is brighter than the synchrotron emission. Therefore, in our approach, we model the sequence of the physical and related radiation processes, and focus on individuating the binary properties that play the relevant roles.

The binary model was proposed in 2012 (Rueda & Ruffini 2012), and it has been in development for one decade. The physical picture and the modeling of the SN ejecta accretion onto the NS companion have been gradually extended to include the required physics, allowing the study of a wide range of binary parameters, based on detailed analysis of multiple well-observed GRBs and statistical analysis of different GRB components (Ruffini et al. 1999, 2000, 2010, 2015; Wang et al. 2015; Ruffini et al. 2018a, 2018b, 2018c; Wang et al. 2018; Ruffini et al. 2019; Wang et al. 2019b; Rueda et al. 2020; Rueda & Ruffini 2020; Moradi et al. 2021b; Ruffini et al. 2021). The numerical simulations of the occurring physical processes have been upgraded from one dimension (Fryer et al. 2014) to two dimensions (Becerra et al. 2015) to three dimensions (Becerra et al. 2016, 2019). The latest simulations (Becerra et al. 2019) implemented a smoothed particle hydrodynamics method, and examined a large selection of the initial conditions and outcomes of the binary system after the SN explosion. Rueda

et al. (2019) and Rueda et al. (2021) have reviewed the entire development process. In this article, we have the scenario—namely, a type II binary-driven hypernova (BdHN II)—that the NS does not accrete enough matter to reach the critical mass for black hole (BH) formation, meaning that it remains stable as a more massive NS (MNS).

Unlike the traditional fireball model, the BdHN model considers a central engine arising in the final evolutionary stage of the CO_{core} in the presence of a binary companion. An SN explosion occurs, which triggers the GRB emission and generates a ν NS. Therefore, in addition to the physical processes of singlestar collapse models, we need to consider not only the binary interactions, but also the appearance of the ν NS. The most influential interactions are the accretion of the SN ejecta onto the NS companion, with the fallback accretion onto the ν NS spinning it up. The afterglow is produced by the mildly relativistic expanding SN ejecta, which contain a large number of electrons accelerated by the kinetic energy of the SN and the energy injection from the rapidly spinning νNS and its subsequent spindown. In this article, we will model the afterglow of GRB 190829A, following the above picture. An additional advantage is that it naturally accounts for the observed association of GRBs with type Ic SNe (Rueda & Ruffini 2012), as well as indicating the peak luminosity of the optical SN emission well above the synchrotron optical emission.

This article is structured as follows. In Section 2, we present the physical picture and the emission episodes that our model predicts. In Section 3, we introduce the observational data. In Section 4, we analyze the prompt emission and explain the prompt pulses by means of the SN explosion and the accretion of SN ejecta onto the companion NS and ν NS. In Section 5, we analyze the afterglow, then model the radio, optical, and X-ray emissions using the synchrotron emission from the SN ejecta. In Section 6, we present the conclusions of the article.

2. Physical Picture and Expectations

As recalled in the introduction, we consider a binary system composed of a CO_{core} and an NS with an orbital period of a few tens of minutes (Ruffini et al. 2021). At a given time, the CO_{core} collapses, forms a νNS at its center, and induces an SN explosion. Most of the SN energy ($\sim 10^{53}$ erg) is deposited in the neutrino, while a small percentage of the energy goes to the kinetic energy of the SN ejecta ($\sim 10^{51}$ – 10^{52} erg), which expands outward at velocities of around 0.1c (Arnett 1996; Branch & Wheeler 2017; Cano et al. 2017). The low-density outermost layer has the highest speed, while the denser regions expand with slower velocities. After a few minutes, the SN ejecta reach the companion NS, and the hypercritical accretion starts. In the meantime, some matter falls back, leading to an accretion process onto the νNS . This fallback accretion is significantly amplified by the companion NS, which alters the trajectory of the partial SN ejecta that flow back to the νNS (Becerra et al. 2019; J. A. Rueda et al. 2022, in preparation). The accretion rate onto the companion NS rises exponentially and peaks in a few minutes. The numerical simulations presented in Fryer et al. (2014), Becerra et al. (2016, 2019), and J. A. Rueda et al. (2022, in preparation) show that the entire hypercritical accretion process may last for hundreds of minutes, while the peak accretion rate of $\sim 10^{-3} M_{\odot} \text{ s}^{-1}$, supplied by the high-density and slow-moving part of the SN ejecta, holds only for tens of seconds to tens of minutes, depending on the binary separation, with the energy release being in the order of 10^{48} – 10^{49} erg s⁻¹. The accretion onto

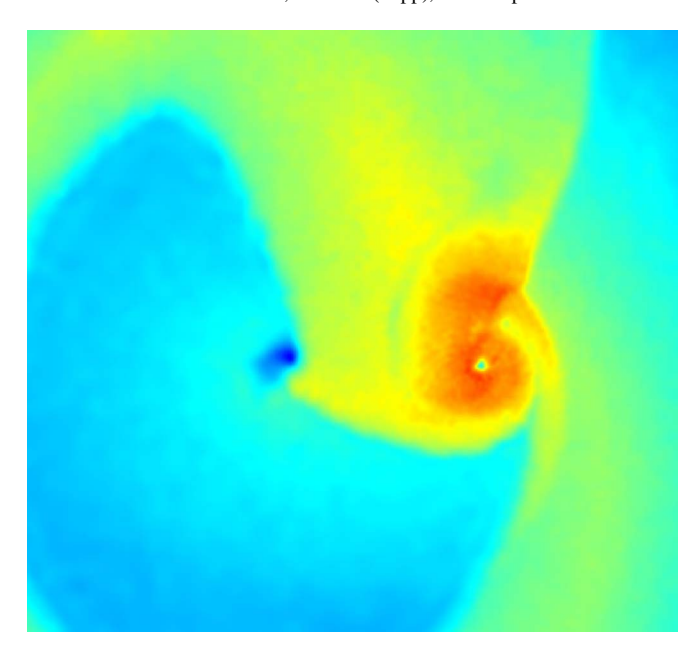


Figure 1. The ongoing accretion process onto the νNS and the NS companion, as simulated in Becerra et al. (2019). The νNS is located at the center of the dark blue spot, and is accreting the surrounding material. The SN ejecta are also being accreted by the NS companion, which is located at the center of the green spot. We also notice that the expansion of the SN ejecta is distorted by the companion NS and that some of the SN ejecta are flowing back to the νNS . This process creates a unique feature of BdHNe: the fallback accretion onto the νNS is enhanced, creating a second peak of accretion at about an orbital period of time after the SN explosion (see, e.g., Figure 5 in Becerra et al. 2019 for more details).

the νNS has two components. The first is the typical fallback matter, analogous to the case of the SN of a single star, which leads the accretion rate to reach a peak, then to decay nearly as a power law with time, $\propto t^{-5/3}$. The peak luminosity produced by it is weak, $<10^{48}$ erg s⁻¹, and can hardly be for cosmological distances. The second component is the unique feature of the binary system that is induced by the interaction of the SN ejecta with the NS companion. The presence of the companion enhances the fallback onto the ν NS, creating a second peak of accretion (Becerra et al. 2019; see, e.g., Figure 1). The second part contributes the most to the accreting mass, with an accretion rate of $\sim 10^{-3} M_{\odot} \text{ s}^{-1}$ at about an orbital period of time after the SN explosion (J. A. Rueda et al. 2022, in preparation). The fallback accretion also transfers angular momentum to the νNS , spinning it up to a rotation period of a few milliseconds (Bhattacharyya & Chakrabarty 2017). The peak luminosity from the fallback accretion is of the order of 10^{48} – 10^{49} erg s⁻¹, and occurs at minutes to tens of minutes after the SN explosion. As we show below, the fallback accretion will continue as a source of energy that powers the afterglow. The SN produces $\sim 0.4~M_{\odot}$ nickel, whose radioactive decay energy is emitted mainly at optical wavelengths, with a corresponding flux that peaks at around \sim 13 days in the source rest-frame (Cano et al. 2017). This optical signal can be observed from some low-redshift sources ($\sim z < 1$) that are less affected by the absorption (Woosley & Bloom 2006).

In summary, from the observational point of view, a few minutes after the SN explosion, we first expect to observe the signal from the accretion onto the companion NS and the ν NS, whose peak times may overlap or be separate, depending on the binary separation, hence there will be one or two pulses with luminosities of the order of 10^{48} erg s⁻¹ to 10^{49} erg s⁻¹. We will then observe the afterglow emission due to the synchrotron emission from the SN ejecta, with a luminosity that decays as a

power law, and at \sim 13 days we will observe an optical bump from the radioactive decay of nickel.

3. Observations

At 19:55:53 UT, on 2019 August 29, GRB 190829A triggered the Fermi-Gamma-Ray Burst Monitor (GBM; Fermi GBM Team 2019). Swift-Burst Alert Telescope (BAT) was triggered 51 s later, but fortunately GRB 190829A was in the Swift-BAT field of view before the trigger. Here, in this paper, we take the GBM trigger time as T_0 . The Swift-X-Ray Telescope (XRT) started to observe at time $T_0 + 148.3$ s (Dichiara et al. 2019). The redshift of $z = 0.0785 \pm 0.005$ was proposed by Swift-UVOT (Dichiara et al. 2019), the Half Meter Telescope (Xu et al. 2019), and the Nordic Optical Telescope (Heintz et al. 2019), via associating to a nearby galaxy, and was later confirmed by the spectroscopic observations of GTC (Hu et al. 2021). GRB 190829A is one of the nearest GRBs ever observed. The SN association has been found and confirmed by the Liverpool Telescope, GTC (Perley & Cockeram 2019; de Ugarte Postigo et al. 2019), and GROND (Bolmer et al. 2019).

We retrieve the Fermi data from the Fermi Science Support Center, ¹⁶ and they were analyzed using the Multi-Mission Maximum Likelihood framework (3ML; Vianello et al. 2015).¹⁷ The spectrum fitting is performed by a Bayesian analysis with Markov Chain Monte Carlo iterations within the 3ML framework, and the results are double-checked by implementing the Fermi GBM Data Tools (Goldstein et al. 2021). For a detailed Bayesian analysis of the data and the reduction procedure applied to a GRB spectrum, we refer to Li et al. (2019), Li (2019a, 2019b), Li et al. (2021), and Li & Zhang (2021). We retrieve the Swift data from the UK Swift Science Data Centre, ¹⁸ and the analyzing and fitting are carried out by HEASoft¹⁹ and 3ML. The VHE data observed by HESS are from Chand et al. (2020), the optical data observed by GTC are taken from Hu et al. (2021), and the radio emission observed by the Arcminute Microkelvin Imager—Large Array (AMI-LA) are taken from Rhodes et al. (2020).

4. Prompt Emission: SN Explosion and NS Accretion

Both the GBM and BAT light curves show two pulses—see, e.g., the Fermi-GBM light curves in Figures 2 and 3. The first pulse starts to rise at time -0.75 s, peaks at 1.02 s, and fades at 8.05 s. The cutoff power-law function gives a best fit over the power law and band functions. We also tested the addition of a blackbody component to the above models, but this did not lead to a statistical improvement of the fit. As shown in Figure 4, the fit of the spectrum is characterized by the power-law index $\alpha = -1.15 \pm 0.06$ and peak energy $E_p = 144.28 \pm 50.67$ keV. The integrated isotropic energy²⁰ from 1 keV to 10 MeV gives $4.25 \pm 1.02 \times 10^{49}$ erg s⁻¹. The averaged luminosity is $4.84 \pm 1.16 \times 10^{48}$ erg s⁻¹. After 38.45 s, the second, larger pulse rises at 46.50 s, peaks at 51.65 s, and fades at 64.00 s. This pulse is best fitted by a band function with a low peak

https://fermi.gsfc.nasa.gov/ssc/

¹⁷ https://threeml.readthedocs.io

¹⁸ https://www.swift.ac.uk

https://heasarc.gsfc.nasa.gov/lheasoft/

 $^{^{20}}$ For the calculation of the luminosity distance, we use a Friedman–Lemaître–Robertson–Walker metric, Hubble constant $H_0=67.4\pm0.5$ km/s/Mpc, and matter density $\Omega_M=0.315\pm0.007$ (Planck Collaboration et al. 2020).

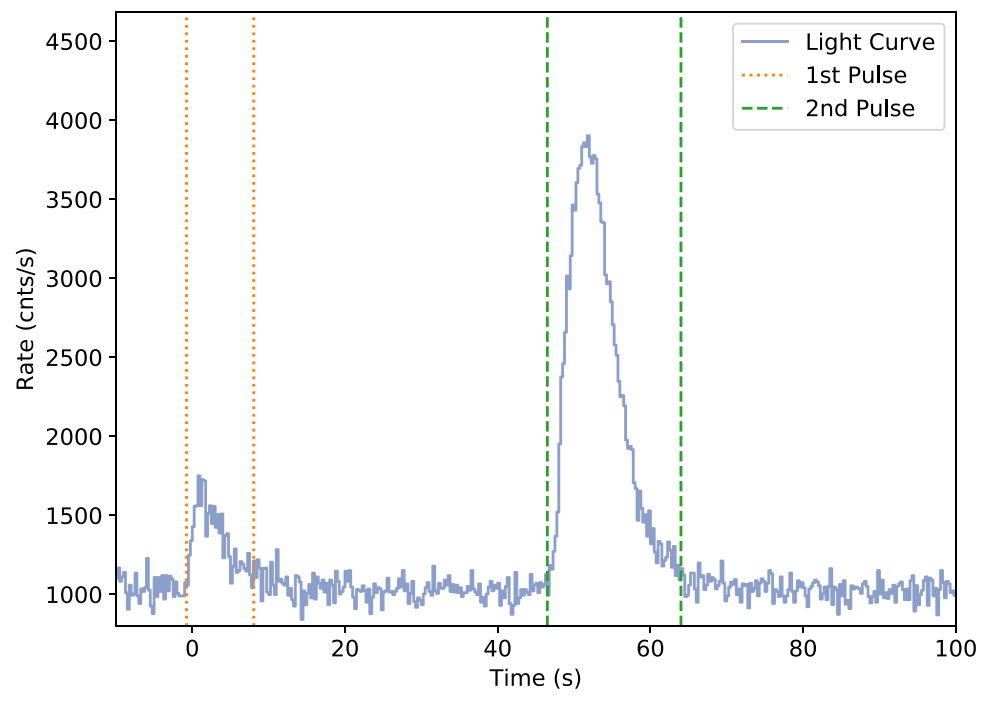


Figure 2. The count rate of the GRB 190829A prompt emission from the raw data of Fermi-GBM: the first pulse is from -0.75 s to 8.05 s, indicated by the orange dotted line, and the second pulse is from 46.50 s to 64.00 s, indicated by the green dashed line.

energy $E_p=13.58\pm0.42$ keV, which almost touches the lower edge of the Fermi-GBM energy band. Because of the small amount of data of energy lower than E_p , the low energy is unconstrained; in fact, we obtain $\alpha=0.50\pm1.01$. The high-energy index $\beta=-2.53\pm0.02$ appears to be a typical value. The total energy in the second pulse is $3.56\pm0.50\times10^{50}$ erg, and the averaged luminosity is $2.05\pm0.29\times10^{49}$ erg s⁻¹. Our spectral fit is consistent with the analysis of Hu et al. (2021).

We interpret these two pulses as being due to the accretion onto the companion NS and the fallback accretion onto the ν NS. The observed energy and luminosity are consistent with our expectation that the emission from the accretion processes with a luminosity of $\sim 10^{48} - \sim 10^{49}$ erg s⁻¹.

Numerical simulations of BdHNe show that the time evolution of the ν NS fallback accretion rate has a two-peak structure, the second peak being a unique feature of the binary interactions, while the accretion onto the MNS companion shows a single-peak structure (see, e.g., Figure 5 in Becerra et al. 2019). The first peak of the ν NS fallback accretion is probably not observable, because, before it occurs, the star has little rotational energy to be released. Therefore, we assume that the two observed pulses are related to the second peak of the νNS accretion and the peak of the MNS accretion. The simulations show that the fallback accretion rate onto the ν NS weakly depends on the binary parameters, while the time of occurrence and intensity of the accretion peak onto the MNS crucially depends on the orbital period and the initial angular momentum of the MNS at the beginning of the accretion. The larger the orbital period, the lower the MNS accretion peak, and the later it occurs, the more it approaches the time of occurrence of the second accretion peak of the ν NS. The relatively short time separation between the two observed peaks in GRB 190829A suggests a binary period of the order of tens of minutes. This is also suggested by the energy released in the emission. For an orbital period in the range of 20-40 minutes, we expect a peak accretion rate of the MNS in the range of 10^{-4} – $10^{-5}M_{\odot}$ s⁻¹ (see Figure 5 in Becerra et al. 2019), which translates into an accretion power of 10^{48} – 10^{49} erg s⁻¹, assuming 10% efficiency in the conversion from gravitational to radiation energy. If we assume that the energy release is powered by the rotational energy gained during the accretion process, then we end up with similar figures. The star gains angular momentum at a rate of $\dot{J}\sim 2\sqrt{3}\,GM\dot{M}/c\sim 4\times 10^{45}\,{\rm g~cm^2~s^{-1}}$, for $1.5M_{\odot}$ and the above accretion rate, which implies a spinup rate of about $40\,{\rm Hz~min^{-1}}$. The simulations show that the MNS accretion peaks at about one-tenth of the orbit, therefore, for the above range of orbital periods, at the time of the accretion the MNS could rotate with a frequency of 80– $160\,{\rm Hz}$, which implies a rotation power of $\Omega\dot{J}\sim (2-5)\times 10^{48}\,{\rm erg~s^{-1}}$, where Ω is the stellar angular velocity.

5. Afterglow: Synchrotron and ν NS Pulsar Radiation

Figure 3 shows the multiwavelength luminosity light curves. We notice the continuity of the Swift-BAT and Swift-XRT observations, and a soft X-ray depression at $\sim\!10^2\!-\!10^3\,\mathrm{s}$ after the prompt emission, then from $3\times10^5\,\mathrm{s}$ the soft X-rays decay as a power law of index -1.26 ± 0.06 . The optical and radio afterglows also have a power-law decay behavior. The VHE emission evolves similarly to the X-rays, with a luminosity of $\sim\!25\%$ of the absorption-corrected X-ray luminosity, similar to other GRBs with VHE observations (Abdalla et al. 2019; MAGIC Collaboration et al. 2019; Zhang 2019; Abdalla et al. 2021).

The optical observations show an additional bump after 10⁶ s (Perley & Cockeram 2019; de Ugarte Postigo et al. 2019), which indicates the SN optical emission powered by nickel decay.

We here follow and extend the treatment of the GRB afterglow by Ruffini et al. (2018a) within the BdHN scenario. In this picture, the afterglow originates from the synchrotron radiation produced by the expansion of the SN ejecta in the presence of the magnetic field of the ν NS. We now estimate the emission generated by the synchrotron mechanism in the X-rays, in the optical, and in the radio, together with the pulsar emission of the ν NS. The ν NS contributes the energy of

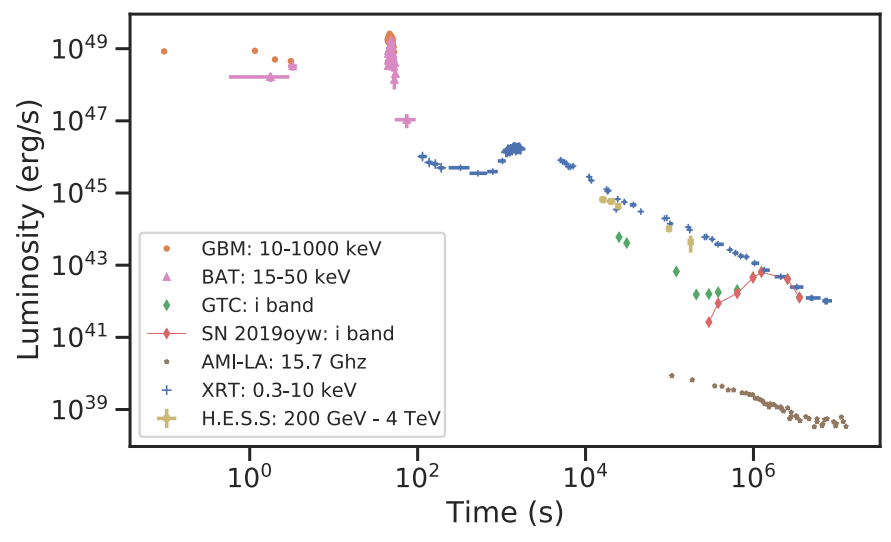


Figure 3. The luminosity of GRB 190829A, including the data from HESS (yellow) for TeV; Fermi-GBM (orange dots); Swift-BAT (purple triangles) for the prompt emission of hard X-rays and gamma-rays; Swift-XRT (blue crosses) for the soft X-rays (absorbed); GTC (green diamonds) for the optical *i* band, from which the SN 2019yw is extracted (red diamonds)—the optical signal of the SN overshoots the synchrotron optical emission; and AMI-LA (brown stars) for the radio observation.

afterglow by two means: first, the fallback accretion of surrounding matter, the energy from which dominates the early afterglow; and second, the release of rotation energy from its spindown, which produces the late-time X-ray afterglow. This model predicts that the VHE emission is not directly emitted by this synchrotron emission, although it seems to be related to the νNS activity (see Section 6).

5.1. Synchrotron Emission by the Expanding Ejecta

Because the electrons lose their energy from synchrotron radiation very efficiently, we can apply a one-zone model, assuming that the radiation originates from the ejecta, say $r = R_*$. We assume that the ejecta expand at a constant velocity $v_{*,0}$, so the radius evolves as

$$R_*(t) = R_{*,0} \,\hat{t},\tag{1}$$

where $\hat{t} \equiv t/t_*$ and $t_* \equiv R_{*,0}/v_{*,0}$.

In agreement with pulsar theory (see, e.g., Goldreich & Julian 1969; Ostriker & Gunn 1969), we assume that, at large distances from the νNS , beyond its light cylinder, the magnetic field decreases linearly with distance. This implies that the magnetic field strength felt by the expanding ejecta evolves with time as

$$B_*(t) = B_{*,0} \frac{R_{*,0}}{R_*} = \frac{B_{*,0}}{\hat{t}},$$
 (2)

where $B_*^{(0)}$ is the magnetic field strength at $r = R_{*,0}$, and we have used Equation (1).

The evolution of the distribution of radiating electrons per unit energy, N(E, t), is obtained from the solution of the well-known classical kinetic equation (see, e.g., Kardashev 1962),

$$\frac{\partial N(E,t)}{\partial t} = -\frac{\partial}{\partial E} [\dot{E} N(E,t)] + Q(E,t), \tag{3}$$

which accounts for the particle energy losses, where Q(E, t) is the number of injected electrons per unit time, per unit energy, and \dot{E} is the electron energy-loss rate. In the present case, the electrons are subjected to adiabatic losses, due to the ejecta expansion, and to synchrotron radiation losses, because of the magnetic field.

Therefore, the electron energy evolves with time, according to the classical energy balance equation (Kardashev 1962):

$$-\dot{E} = \frac{E}{t} + P_{\text{syn}}(E, t), \tag{4}$$

where

$$P_{\rm syn}(E, t) = \beta B_*^2(t) E^2 \tag{5}$$

is the bolometric synchrotron power and $\beta = 2e^4/(3m_e^4c^7)$ (for details, see, e.g., Longair 2011).

We adopt a distribution of the injected particles following a power-law behavior (see, e.g., Kardashev 1962; Rybicki & Lightman 1979; Longair 2011):

$$Q(E, t) = Q_0(t)E^{-\gamma}, \ 0 \leqslant E \leqslant E_{\text{max}}, \tag{6}$$

where γ and $E_{\rm max}$ are parameters to be determined from the observational data. We now address the function determining the rate of particle injection, $Q_0(t)$, which is related to the power injected by the $\nu {\rm NS}$ into the ejecta, i.e., the injected electrons are accelerated by the energy from the fallback accretion onto the $\nu {\rm NS}$. We assume that the bolometric power released by the $\nu {\rm NS}$ is given by

$$L_{\rm inj}(t) = L_0 \left(1 + \frac{t}{t_q} \right)^{-k},$$
 (7)

where L_0 , t_q , and k are model parameters. Because the ejecta surround the νNS , the power released by the νNS is injected into the ejecta, so the function $Q_0(t)$ can be found from energy conservation as

$$L_{\rm inj}(t) = \int_0^{E_{\rm max}} E \, Q(E, t) dE = Q_0(t) \frac{E_{\rm max}^{2-\gamma}}{2-\gamma}, \tag{8}$$

which, via Equation (7), leads to

$$Q_0(t) = q_0 \left(1 + \frac{t}{t_q} \right)^{-k}, \tag{9}$$

where $q_0 \equiv (2 - \gamma)L_0/E_{\text{max}}^{2-\gamma}$.

With the specification of the ejecta evolution given by Equation (1), that of the magnetic field given by Equation (2), and the rate of particle injection given by Equations (6) and (9),

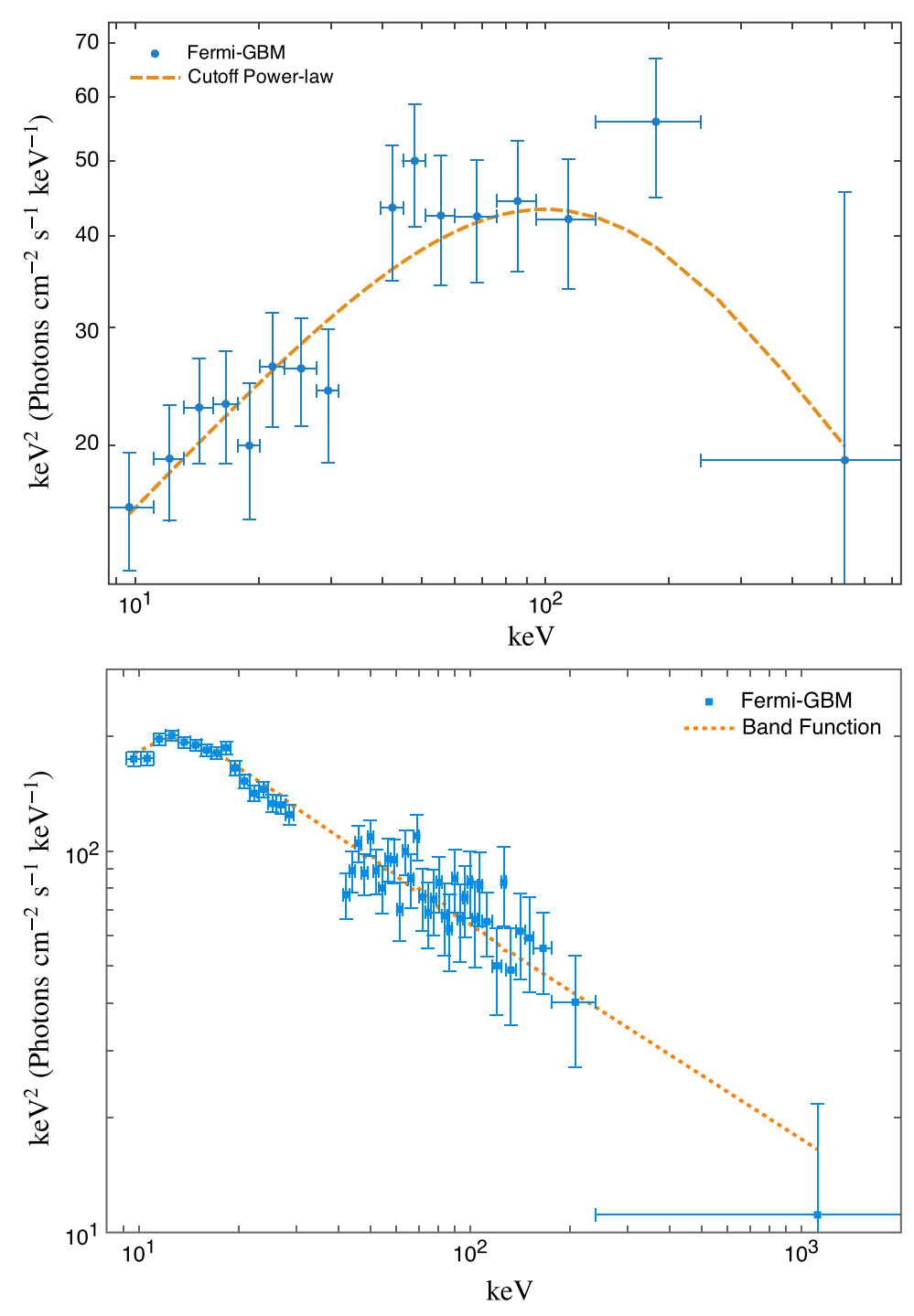


Figure 4. Top: the spectrum of the first pulse observed by Fermi-GBM. The blue points are the data and the orange curve indicates the fitting by a cutoff power law with power-law index $\alpha = -1.45$ and the peak energy $E_p = 144.28$ keV. Bottom: the spectrum of the second pulse. The blue points are the data and the orange curve indicates a band function fitting, with the low-energy index $\alpha = 0.50$, the high-energy index $\beta = -2.53$, and the peak energy $E_p = 13.58$ keV.

we proceed to integrate the kinetic Equation (3). For this task, we must first find the time evolution of the energy of a generic electron injected at time $t = t_i$ with initial energy E_i . With all the above, Equation (4) is a Riccati differential equation that has the following analytic solution (Rueda et al. 2022; Rueda 2022):

$$E = \frac{E_i(t_i/t)}{1 + \mathcal{M}E_i t_i \left(\frac{1}{\hat{t}_i^2} - \frac{1}{\hat{t}^2}\right)},$$
 (10)

where $\mathcal{M} \equiv \beta B_{*,0}^2/2$.

Following Pacini & Salvati (1973), we write the solution to Equation (3) as

$$N(E, t) = \int_{E}^{\infty} Q[E_i, t_i(t, E_i, E)] \frac{\partial t_i}{\partial E} dE_i,$$
 (11)

where $t_i(t, E_i, E)$ is obtained from Equation (10). The solution N(E, t) can be written as a piecewise function of time, depending upon the behavior of the energy injection in Equation (9); i.e., at times $t < t_q$, it can be approximated as a constant, while at longer times it is well approximated by a

pure power-law function. In addition, as we shall show below, the GRB afterglow data is well explained by a regime in which synchrotron radiation losses dominate over adiabatic losses. Under these conditions, the solution of Equation (11) can be written as (Rueda et al. 2022)

$$N(E, t) \approx \begin{cases} \frac{q_0}{\beta B_{*,0}^2(\gamma - 1)} \hat{t}^2 E^{-(\gamma + 1)}, & t < t_q \\ \frac{q_0 (t_q / t_*)^k}{\beta B_{*,0}^2(\gamma - 1)} \hat{t}^{2-k} E^{-(\gamma + 1)}, & t_q < t < t_b, \end{cases}$$
(12)

where the electron energy is in the range $E_b < E < E_{\text{max}}$, being

$$E_b = \frac{\hat{t}}{\mathcal{M}t_*}, \quad t_b = t_*^2 \mathcal{M} E_{\text{max}}. \tag{13}$$

The synchrotron luminosity radiated in the frequencies $[\nu_1, \nu_2]$ can then be obtained as

$$L_{\text{syn}}(\nu_1, \nu_2; t) = \int_{\nu_1}^{\nu_2} J_{\text{syn}}(\nu, t) d\nu, \tag{14}$$

where $J_{\rm syn}(\nu,t)$ is the synchrotron spectral density (energy per unit time, per unit frequency), $\nu_1 = \nu$, and $\nu_2 = \nu + \Delta \nu$, with $\Delta \nu$ being the bandwidth. The synchrotron power is mostly emitted at radiation frequencies close to the so-called critical frequency $\nu_{\rm crit} = \alpha B_* E^2$, where $\alpha = 3e/(4\pi m_e^3 c^5)$ (see, e.g., Rybicki & Lightman 1979). Therefore, the bolometric synchrotron power of Equation (5) can be readily written in terms of the radiation frequency ν as

$$P_{\text{syn}}(E, t) \approx P_{\text{syn}}(\nu, t) = \frac{\beta}{\alpha} B_* \nu = \frac{\beta}{\alpha} \frac{B_{*,0}}{\hat{t}} \nu,$$
 (15)

and, within the same approximation (see, e.g., Longair 2011),

$$J_{\text{syn}} d\nu \approx P_{\text{syn}}(\nu, t) N(E, t) dE.$$
 (16)

We now replace this into Equation (14) and obtain the synchrotron luminosity

$$L_{\text{syn}}(\nu, t) = \frac{\beta}{2} \alpha^{\frac{p-3}{2}} \eta B_{*,0}^{\frac{p+1}{2}} \hat{t}^{\frac{2l-p-1)}{2}} \nu^{\frac{3-p}{2}}, \tag{17}$$

where we have used the approximation $\Delta\nu/\nu\ll 1$ in the integration of Equation (14) in view of the power-law behavior of $J_{\rm syn}$, and we have written the electron distribution as $N(E,t)=\eta~\hat{t}^lE^{-p}$, with η , l, and p being known constants from Equation (12).

Therefore, the synchrotron power has a power-law dependence in both time and radiation frequency; see Equation (17). If, over time, the system remains in the same physical regime in which the energy losses of the electrons are dominated by synchrotron radiation, the luminosities in the X-ray, optical, and radio wavelengths decrease with the same power-law index (see Figure 5). For the parameters of GRB 190829A (see Table 1), we found that this condition is fulfilled; i.e., the afterglow data remains at times $t < t_b$ and is explained by electron energies that hold in the range $E_b < E < E_{\rm max}$ —see Equation (13). In this case, the ratio of the synchrotron luminosity at different frequencies is constant in time, because it depends only on the power-law

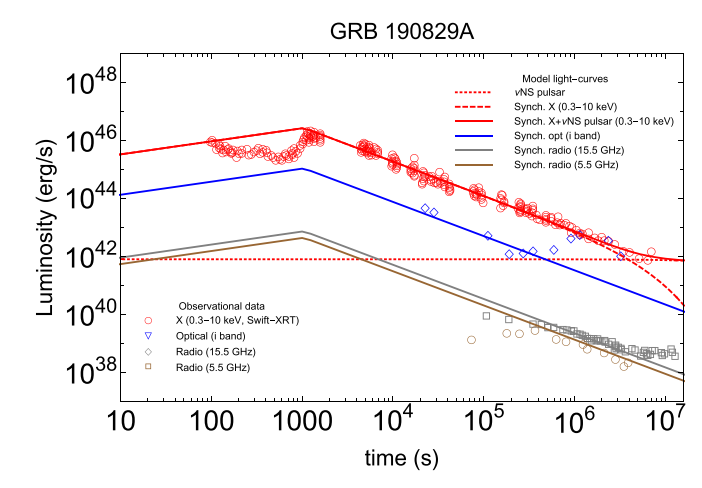


Figure 5. The luminosity of GRB 190829A in the X-ray (0.3–10 keV), optical (*i* band; Hu et al. 2021), and radio (5.5 and 15.5 GHz) energy bands (Rhodes et al. 2020).

Table 1
Numerical Values of the Theoretical Model of Synchrotron Radiation that Fit the Multiwavelength Observational Data of GRB 190829A, as Shown in Figure 5

Parameter	Value
$\frac{\gamma}{\gamma}$	1.01
k	1.63
$L_0 (10^{46} \text{ erg s}^{-1})$	8.00
$E_{\rm max} \ (10^4 \ m_e c^2)$	5.00
t_q (s)	1050.00
$R_{*,0}$ (10 ¹¹ cm)	1.00
$v_{*,0} (10^9 \text{ cm s}^{-1})$	1.00
$B_{*,0} (10^6 \text{ G})$	5.01
ξ	100.00
$B_{\rm dip} \ (10^{12} \ {\rm G})$	5.00
P (ms)	8.00

index of the injection rate as (Rueda 2022)

$$\frac{L_{\text{syn}}(\nu_1, t)}{L_{\text{syn}}(\nu_2, t)} = \left(\frac{\nu_1}{\nu_2}\right)^{\frac{3-p}{2}} = \left(\frac{\nu_1}{\nu_2}\right)^{\frac{2-\gamma}{2}}.$$
 (18)

In practice, we fix the value of γ from the X-rays to the optical luminosity ratio. Having fixed γ , the ratio of the optical (or X-rays) to radio luminosity is fixed, too. Figure 5 shows that this procedure leads to a synchrotron luminosity in the radio band that also agrees with the observations. This result implies that this model correctly describes the afterglow in the wide range of energies, including the radio and the optical, in addition to X-rays, giving strong support to the proposed scenario for afterglow emission.

5.2. vNS Evolution and Pulsar Emission

As the synchrotron luminosity fades with time, the pulsar-like emissions of the νNS and the MNS companion become observable in the X-ray afterglow. We expect the magnetic field of the younger νNS to dominate over that of the much older MNS companion. By the time of the BdHN event, the MNS magnetic field could have decayed with respect to its

birth value. Although microphysical mechanisms leading to magnetic field decay in pulsars have been debated, a relevant mechanism for such a decay is that, during the evolution, the binary passes through common envelope and X-ray binary phases, in which the magnetic field is reduced by long-term accretion episodes (see, e.g., Payne & Melatos 2007, and references therein, for numerical simulations).

Bearing the above in mind, we assume that the pulsar emission observable in the afterglow is driven by the magnetic field of the ν NS. We calculate this pulsar emission following the dipole + quadrupole magnetic field model presented in Pétri (2015). The total pulsar (spindown) luminosity is obtained by summing the dipole and quadrupole contributions:

$$L_{\text{sd}} = L_{\text{dip}} + L_{\text{quad}}$$

$$= \frac{2}{3c^3} \Omega^4 B_{\text{dip}}^2 R^6 \sin^2 \chi_1 \left(1 + \xi^2 \frac{16}{45} \frac{R^2 \Omega^2}{c^2} \right), \tag{19}$$

with R being the νNS radius and ξ defining the quadrupole-to-dipole strength ratio

$$\xi \equiv \sqrt{\cos^2 \chi_2 + 10 \sin^2 \chi_2} \frac{B_{\text{quad}}}{B_{\text{dip}}},\tag{20}$$

where the modes can be separated as: $\chi_1=0$ and any value of χ_2 for the m=0 mode; $(\chi_1,\ \chi_2)=(90^\circ,\ 0^\circ)$ for the m=1 mode; and $(\chi_1,\ \chi_2)=(90^\circ,\ 90^\circ)$ for the m=2 mode.

The evolution of the νNS is calculated by integrating the energy balance equation,

$$-(\dot{W} + \dot{T}) = L_{\text{tot}} = L_{\text{ini}} + L_{\text{sd}},$$
 (21)

where W and T are, respectively, the νNS gravitational and the rotational energy.

Table 1 lists the model parameters that fit the afterglow of GRB 190829A in the X-ray, optical (Hu et al. 2021), and radio energy bands (Rhodes et al. 2020), as shown in Figure 5. The power-law luminosity observed in the multiwavelength data after 10³ s is well explained by the synchrotron emission. We do not find evidence up to times of 10⁷ s of a change in the power-law index, which implies that the system up to these times has not yet transitioned to the physical regime of the dominance of adiabatic losses over synchrotron losses. Although there is a good agreement of the model with the data after 10^3 s, the fit of the emission $<10^3$ s is complicated. At those times, the behavior of the light curve is far from smooth, which is likely due to factors other than the synchrotron alone. The modeling of this early part of the afterglow is challenging for the presently simplified synchrotron picture, and probably needs very detailed information on the density profile of the ejecta and the absorption processes that we are not considering. The light curve at early times may catch short-timescale details of the evolution, so the accurate evaluation of the absorption and/or scattering processes (e.g., synchrotron self-absorption or Thomson scattering), leading to the evolution of the optical depth, might need a detailed radiative-transfer calculation, including possible deviations of the density and the expansion velocity from spherical symmetry (e.g., polar-angle dependence and filaments arising from Rayleigh-Taylor instability) and/or possible deviations of the thermodynamics variables (e.g., temperature and composition) that are needed for the evaluation of the opacity at every photon energy, position, and time. In addition, the early evolution of the ν NS could be highly complex, leading to

an energy injection that deviates from the law assumed in Equation (7). The latter implies a constant injection rate at times $t \lesssim \tau_q \approx 10^3 \, \mathrm{s}$ (see Table 1), leading to the rising synchrotron luminosity following a power law at those times (see Figure 5).

The VHE emission observed in the 0.2–4 TeV energy band of HESS is not explained by the above synchrotron model. We now estimate whether the SSC radiation could originate such an emission. The SSC emission is produced by synchrotron photons that upscatter off the relativistic electrons that produce them. The upscattering increases the energy of those photons by a factor equal to the square of the electron Lorentz factor, leading to a spectrum with a shape similar to the synchrotron spectrum, but at higher energies (Dermer & Menon 2009; Zhang 2018; Wang et al. 2019a; Nigro et al. 2022). Figure 6 shows as an example the first observational epoch of HESS $(17438.5 \pm 805.5 \text{ s})$ and our estimate of the SSC emission for the parameters of our synchrotron model. The SSC emission peaks at a few hundreds of MeV, cuts off at<10 GeV, and has a lower luminosity with respect to that observed in the HESS energy bandwidth. Therefore, we conclude that neither the synchrotron nor the SSC radiation explain the VHE emission of GRB 190829A as observed by HESS. However, the similar power-law behavior of the VHE and the X-ray light curves suggests that the former could be related to some (presently unexplored) transient activity of the νNS . We notice that the HESS team expressed a similar conclusion, that the traditional afterglow model, including SSC radiation, does not explain their observations, and they expected a multizone emission model (Abdalla et al. 2021).

We turn now to the synchrotron emission. The critical synchrotron radiation energy ($h\nu_{\rm crit}$) decreases with time, so the peak of the synchrotron radiation shifts to lower energies with time. Around 10^6 s, the critical radiation energy falls below the keV range, leading to the exponential decay of the synchrotron emission in the X-rays after that time. Subsequently, the pulsar emission from the ν NS dominates the observed X-ray emission. We have taken advantage of this behavior to infer the strength of the dipole and quadrupole components of the magnetic field, as well as the rotational period of the ν NS.

The bump observed in the optical data at about 10^6 s is explained by the SN emission powered by the energy released from nickel decay (Arnett 1996), where, in this specific GRB, the type Ic SN 2019oyw optical signal overshoots the synchrotron optical emission. For the detailed SN observations and analysis, we refer the reader to the article from GTC (Hu et al. 2021).

The radio emission shows some excess over the synchrotron emission, from a few 10^6 s to 10^7 s. This feature may be a signature from the νNS pulsar, although further observational data and theoretical analysis are needed to confirm this hypothesis.

6. Discussion and Conclusion

The BdHN scenario describes the late evolution of a CO_{core} -NS binary. In particular, it predicts the electromagnetic signals that can be observed from a sequence of episodes that are triggered when the CO_{core} undergoes gravitational collapse at the end of its thermonuclear evolution, generating an SN and forming a ν NS at its center. The ejected material from the SN accretes onto the companion NS and also onto the ν NS, via matter fallback. The fate of the

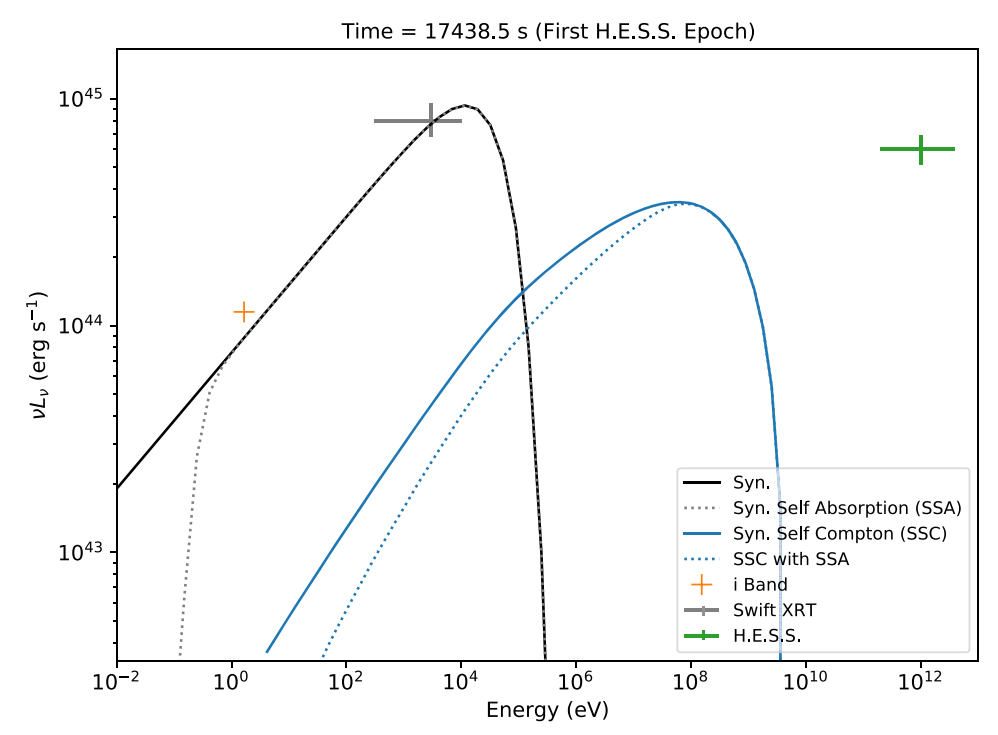


Figure 6. The synchrotron and SSC spectra of the first HESS observational epoch. The synchrotron spectrum well fits the optical and X-ray data. Neither the synchrotron nor the SSC spectra are able to reproduce the HESS observations.

companion NS depends on the initial mass and, crucially, on the binary separation (i.e., the orbital period) that sets the accretion rate. BdHNe I are characterized by short orbital periods of the order of a few minutes, where the NS reaches by accretion the critical mass for gravitational collapse into a BH. We refer the reader to Ruffini et al. (2021) for a comprehensive analysis of 380 BdHN I. In this article, we have analyzed GRB 190829A, which is classified as a BdHN II. These sources are characterized by longer orbital periods, i.e., larger binary separations, with lower accretion rates, and therefore the companion NS does not reach the critical mass for gravitational collapse.

GRB 190829A, at the close distance of redshift 0.0785, was observed by multiband telescopes and satellites on the ground and in space. These detailed observations have given us the opportunity to find the emissions that correspond to the episodes that are expected to occur in a BdHN II. The initial X-ray pulse of energy \sim 4.25 \times 10 49 erg and the second pulse of energy \sim 3.56 \times 10 erg represent the accretion of the SN ejecta onto the companion NS and the ν NS; see Figures 2 and 4 for their light curves and spectra.

We explained the radio, optical, and X-ray afterglow emissions as being due to the synchrotron radiation from the SN ejecta expanding into the magnetic field of the ν NS. The ν NS continuously injects energy into the SN ejecta, from fallback accretion and spindown, owing to magnetic braking. From the fitting of afterglow synchrotron emission—see Figure 5—we infer the ν NS spinning at an 8 ms period, with a dipole field of 5×10^{12} G. The observed VHE emission is explained neither by this synchrotron radiation process nor by SSC radiation. However, the fact that the VHE light curve shows a similar power-law decay to the X-rays, with a lower luminosity being released, but at higher photon energy, is suggestive of a process relating to a transient activity of the ν NS, e.g., glitches, which shares a portion of the rotational

energy and leads to a narrow-angle emission near the light cylinder. The modeling of such a complex physical phenomenon needs further theoretical work and simulations, and, as such, goes beyond the scope of the present article. This same VHE emission parallel to the X-ray afterglow has also been observed in GRB 180720B (Moradi et al. 2021a) and GRB 190114C (R. Ruffini et al., to be submitted).

The BdHN model naturally contains an SN, and indeed in GRB 190829A the SN association was observed. The peak of the SN standard optical luminosity (R. Moradi et al., to be submitted) is higher than the synchrotron optical emission—see Figure 3—which makes the optical SN signal distinguishable.

In general, this article presents an evolutionary picture of the late stage of a binary system, which produces a GRB induced by an SN. We have observed two pulses of luminosity $\sim\!10^{49}~{\rm erg~s}^{-1}$ from the accretion of the SN ejecta onto the NS and the $\nu{\rm NS}$, as well as the NS spindown. From the observations, we infer that the $\nu{\rm NS}$ has an initial spin of 8 ms and a dipole magnetic field $5\times10^{12}~{\rm G}$.

Y.A. acknowledges funding from the Science Committee of the Ministry of Education and Science of the Republic of Kazakhstan (grant No. AP08855631).

ORCID iDs

Yu Wang https://orcid.org/0000-0001-7959-3387 R. Ruffini https://orcid.org/0000-0003-0829-8318 R. Moradi https://orcid.org/0000-0002-2516-5894 Liang Li https://orcid.org/0000-0002-1343-3089 N. Sahakyan https://orcid.org/0000-0003-2011-2731

References

Abdalla, H., Adam, R., Aharonian, F., et al. 2019, Natur, 575, 464 Abdalla, H., Aharonian, F., Benkhali, F. A., et al. 2021, Sci, 372, 1081

```
Arnett, D. 1996, Supernovae and Nucleosynthesis: An Investigation of the
   History of Matter from the Big Bang to the Present (Princeton, NJ:
   Princeton Univ. Press)
Becerra, L., Bianco, C. L., Fryer, C. L., Rueda, J. A., & Ruffini, R. 2016, ApJ,
  833, 107
Becerra, L., Cipolletta, F., Fryer, C. L., Rueda, J. A., & Ruffini, R. 2015, ApJ,
   812, 100
Becerra, L., Ellinger, C. L., Fryer, C. L., Rueda, J. A., & Ruffini, R. 2019, ApJ,
   871.14
Bhattacharyya, S., & Chakrabarty, D. 2017, ApJ, 835, 4
Bolmer, J., Greiner, J., & Chen, T. W. 2019, GCN, 25651, 1
Branch, D., & Wheeler, J. C. 2017, Supernova Explosions (Berlin: Springer)
Cano, Z., Wang, S.-Q., Dai, Z.-G., & Wu, X.-F. 2017, AdAst, 2017, 8929054
Chand, V., Banerjee, A., Gupta, R., et al. 2020, ApJ, 898, 42
de Ugarte Postigo, A., Izzo, L., Thoene, C. C., et al. 2019, GCN, 25677, 1
Dermer, C. D., & Menon, G. 2009, High Energy Radiation from Black Holes:
   Gamma Rays, Cosmic Rays, and Neutrinos (Princeton, NJ: Princeton Univ.
   Press)
Dichiara, S., Bernardini, M. G., Burrows, D. N., et al. 2019, GCN, 25552, 1
Dichiara, S., Troja, E., Lipunov, V., et al. 2021, MNRAS, 512, 2337
Fermi GBM Team 2019, GCN, 25551, 1
Fraija, N., Veres, P., Beniamini, P., et al. 2021, ApJ, 918, 12
Fryer, C. L., Rueda, J. A., & Ruffini, R. 2014, ApJL, 793, L36
Goldreich, P., & Julian, W. H. 1969, ApJ, 157, 869
Goldstein, A., Cleveland, W. H., & Kocevski, D. 2021, Fermi GBM Data
   Tools: v1.1.0, https://fermi.gsfc.nasa.gov/ssc/data/analysis/gbm
Heintz, K. E., Fynbo, J. P. U., Jakobsson, P., et al. 2019, GCN, 25563, 1
Hu, Y. D., Castro-Tirado, A. J., Kumar, A., et al. 2021, A&A, 646, A50
Kardashev, N. S. 1962, SvA, 6, 317
Li, L. 2019a, ApJS, 242, 16
Li, L. 2019b, ApJS, 245, 7
Li, L., Ryde, F., Pe'er, A., Yu, H.-F., & Acuner, Z. 2021, ApJS, 254, 35
Li, L., & Zhang, B. 2021, ApJS, 253, 43
Li, L., Geng, J.-J., Meng, Y.-Z., et al. 2019, ApJ, 884, 109
Longair, M. S. 2011, High Energy Astrophysics (Cambridge: Cambridge Univ.
   Press)
MAGIC Collaboration, Acciari, V. A., Ansoldi, S., et al. 2019, Natur, 575, 455
Mészáros, P. 2002, ARA&A, 40, 137
Moradi, R., Li, L., Rueda, J. A., et al. 2021a, arXiv:2103.09158
Moradi, R., Rueda, J. A., Ruffini, R., & Wang, Y. 2021b, A&A, 649, A75
Nigro, C., Sitarek, J., Gliwny, P., et al. 2022, A&A, 660, A18
Ostriker, J. P., & Gunn, J. E. 1969, ApJ, 157, 1395
```

Pacini, F., & Salvati, M. 1973, ApJ, 186, 249

```
Payne, D. J. B., & Melatos, A. 2007, MNRAS, 376, 609
Perley, D. A., & Cockeram, A. M. 2019, GCN, 25657, 1
Pétri, J. 2015, MNRAS, 450, 714
Piran, T. 2004, RvMP, 76, 1143
Planck Collaboration, Aghanim, N., Akrami, Y., et al. 2020, A&A, 641, A6
Rhodes, L., van der Horst, A. J., Fender, R., et al. 2020, MNRAS, 496
  3326
Rueda, J. A. 2022, arXiv:2202.00316
Rueda, J. A., & Ruffini, R. 2012, ApJL, 758, L7
Rueda, J. A., & Ruffini, R. 2020, EPJC, 80, 300
Rueda, J. A., Ruffini, R., Karlica, M., Moradi, R., & Wang, Y. 2020, ApJ,
  893, 148
Rueda, J. A., Ruffini, R., Li, L., et al. 2022, IJMPD, 31, 2230013
Rueda, J. A., Ruffini, R., Moradi, R., & Wang, Y. 2021, IJMPD, 30, 2130007
Rueda, J. A., Ruffini, R., & Wang, Y. 2019, Univ, 5, 110
Ruffini, R., Karlica, M., Sahakyan, N., et al. 2018a, ApJ, 869, 101
Ruffini, R., Salmonson, J. D., Wilson, J. R., & Xue, S. S. 1999, A&A, 350
  334
Ruffini, R., Salmonson, J. D., Wilson, J. R., & Xue, S.-S. 2000, A&A, 359,
  855
Ruffini, R., Vereshchagin, G., & Xue, S. 2010, PhR, 487, 1
Ruffini, R., Wang, Y., Enderli, M., et al. 2015, ApJ, 798, 10
Ruffini, R., Wang, Y., Aimuratov, Y., et al. 2018b, ApJ, 852, 53
Ruffini, R., Becerra, L., Bianco, C. L., et al. 2018c, ApJ, 869, 151
Ruffini, R., Moradi, R., Rueda, J. A., et al. 2019, ApJ, 886, 82
Ruffini, R., Moradi, R., Rueda, J. A., et al. 2021, MNRAS, 504, 5301
Rybicki, G. B., & Lightman, A. P. 1979, Radiative Processes in Astrophysics
  (New York: Wiley)
Sato, Y., Obayashi, K., Yamazaki, R., Murase, K., & Ohira, Y. 2021, MNRAS,
  504, 5647
Vianello, G., Lauer, R. J., Younk, P., et al. 2015, arXiv:1507.08343
Wang, X.-Y., Liu, R.-Y., Zhang, H.-M., Xi, S.-Q., & Zhang, B. 2019a, ApJ,
  884, 117
Wang, Y., Aimuratov, Y., Moradi, R., et al. 2018, MmSAI, 89, 293
Wang, Y., Rueda, J. A., Ruffini, R., et al. 2019b, ApJ, 874, 39
Wang, Y., Ruffini, R., Kovacevic, M., et al. 2015, ARep, 59, 667
Woosley, S. E., & Bloom, J. S. 2006, ARA&A, 44, 507
Xu, D., Yu, B. Y., Zhu, Z. P., et al. 2019, GCN, 25555, 1
Zhang, B. 2018, The Physics of Gamma-ray Bursts (Cambridge: Cambridge
  Univ. Press)
Zhang, B. 2019, Natur, 575, 448
Zhang, B. T., Murase, K., Veres, P., & Mészáros, P. 2021a, ApJ, 920, 55
Zhang, L.-L., Ren, J., Huang, X.-L., et al. 2021b, ApJ, 917, 9
```